

A Hierarchical Map of Regulatory Genetic Interactions in Membrane Trafficking

Prisca Liberali,^{1,*} Berend Snijder,^{1,2} and Lucas Pelkmans^{1,*}

¹Institute of Molecular Life Sciences, University of Zurich, Winterthurerstrasse 190, 8057 Zürich, Switzerland

²Present address: CeMM-Research Center for Molecular Medicine of the Austrian Academy of Sciences, 1090 Vienna, Austria

*Correspondence: prisca.liberali@uzh.ch (P.L.), lucas.pelkmans@imls.uzh.ch (L.P.)

<http://dx.doi.org/10.1016/j.cell.2014.04.029>

SUMMARY

Endocytosis is critical for cellular physiology and thus is highly regulated. To identify regulatory interactions controlling the endocytic membrane system, we conducted 13 RNAi screens on multiple endocytic activities and their downstream organelles. Combined with image analysis of thousands of single cells per perturbation and their cell-to-cell variability, this created a high-quality and cross-comparable quantitative data set. Unbiased analysis revealed emergent properties of the endocytic membrane system and how its complexity evolved and distinct programs of regulatory control that coregulate specific subsets of endocytic uptake routes and organelle abundances. We show that these subset effects allow the mapping of functional regulatory interactions and their interaction motifs between kinases, membrane-trafficking machinery, and the cytoskeleton at a large scale, some of which we further characterize. Our work presents a powerful approach to identify regulatory interactions in complex cellular systems from parallel single-gene or double-gene perturbation screens in human cells and yeast.

INTRODUCTION

Endocytosis mediates nutrient uptake, remodels the cell surface, and is the prime portal for pathogen entry (Conner and Schmid, 2003). It comprises multiple mechanisms to internalize cell-surface components and extracellular fluid (Doherty and McMahon, 2009) and various downstream organelles to dynamically process or recycle the internalized material (Maxfield and McGraw, 2004). Because actively growing cells in tissue culture internalize and recycle more than 200% of their entire surface area every hour (Steinman et al., 1983), endocytosis has a major role in cell signaling, cell-cell communication, and interactions between cells and their environment (Scita and Di Fiore, 2010). Given its essential role, endocytosis is itself subject to extensive and complex regulation (Liberali et al., 2008), whose scope has been revealed by a number of large-scale efforts to annotate human

gene function to endocytosis (Collinet et al., 2010; Galvez et al., 2007; Kozik et al., 2013; Pelkmans et al., 2005). However, no systematic study has been undertaken to compare the regulation of different endocytic activities and organelles, and most of the signaling networks that control them remain unknown. It is unclear whether patterns of coordination exist. Moreover, large-scale maps of functional interactions between molecular components of different endocytic machineries and cellular signaling do not exist.

Genetic perturbation screens combined with data-driven statistics to infer functional genetic interactions are powerful methods for the unbiased, large-scale, and quantitative analysis of molecular complexes. These interactions can be inferred from large sets of single gene perturbation screens with a quantitative readout (Hillenmeyer et al., 2008; Steinmetz et al., 2002) and from double-gene perturbation screens to measure synthetic interactions (Costanzo et al., 2010; Schuldiner et al., 2005). However, such approaches have thus far not been able to accurately reveal molecular regulatory circuits involving, for instance, kinase-substrate interactions, because of a poor correlation between their perturbation effects across a large number of measurements (Fiedler et al., 2009). In addition, in human cells, large-scale double-gene perturbation screens suffer from poor scalability and are technically challenging (Bassik et al., 2013; Laufer et al., 2013; Roguev et al., 2013). Therefore, most screens have been based on single-gene knockdowns with RNAi and thus do not reveal functional linkages between cellular processes.

Here, we developed a quantitative approach based on parallel RNAi screens and a statistical method to infer functional regulatory interactions between genes. Using this methodology, we analyzed the loss-of-function phenotypes of 13 different, but functionally related, endocytic activities and organelles in human cells to infer functional interactions between genes. The set of targeted genes covers the known molecular components of several endocytic machineries, as well as genes involved in signaling and the cytoskeleton. Our approach is quantitative at the level of single cells and takes patterns of cell-to-cell variability into account to avoid sampling bias and misinterpretations due to indirect population-context effects. The acquired data set facilitated the unbiased discovery of unknown systems-level properties that conventional approaches cannot reveal. We find specific regulatory programs that coordinate subsets of endocytic activities and organelle abundances

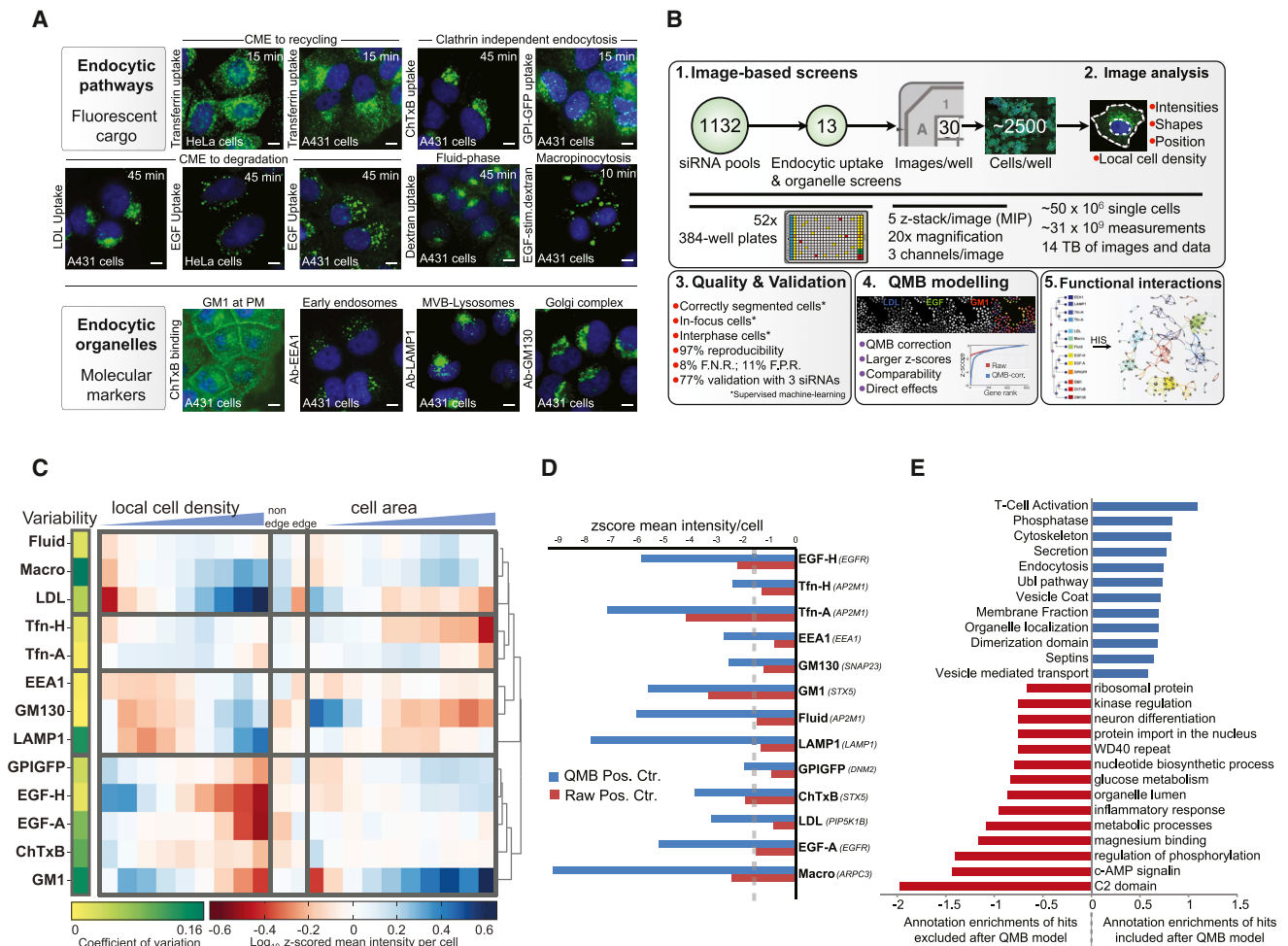


Figure 1. Overview of the Workflow and Patterns of Cell-to-Cell Variability in the Endocytic Membrane System

(A) Example images of single cells from the 13 automated image-based assays using fluorescent cargo. Scale bars, 10 μ m.

(B) Overview of the experimental and computational workflow of the RNAi screens analyzed in this study.

(C) Analysis and population context-determined patterns of cell-to-cell variability. Left column: coefficients of variation (CoV) of single-cell fluorescent cargo or molecular marker intensities (\log_{10} -transformed mean intensity). Bootstrapped hierarchical clustering of cell-to-cell variability patterns. Intensity was calculated per bin of the quantile multidimensional bin (QMB) model.

(D) Correction with QMB models improves the Z scores of positive controls.

(E) Accounting for indirect population-context effects leads to changes in the enrichments of functional annotation classes of hits. Bar graph shows functional annotation classes, which become depleted (red, on the left) or enriched (blue, on the right) after QMB model correction.

See also Figure S1.

controlling the core membrane-trafficking machinery on which these activities rely and harness subset effects in the data to map the functional interactions between signaling, membrane trafficking, and cytoskeletal genes underlying these regulatory programs. We show the generality of our approach and its applicability to other complex cellular processes by inferring regulatory interactions from subset effects in a *Saccharomyces cerevisiae* double-gene perturbation screen. Finally, we characterize some of the identified functional interactions in the regulation of clathrin-mediated endocytosis with automated total internal reflection fluorescence (TIRF) time-lapse microscopy and large-scale image analysis on genome-edited cells, further validating the discovery approach developed in this resource.

RESULTS

Thirteen Image-Based RNAi Screens of Endocytic Activities and Organelles

To reveal coordinate and disparate regulation of the multiple endocytic pathways that converge on the endolysosomal system, we designed 13 high-throughput image-based assays, which measure different endocytic activities, as well as the abundance of endosomes, lysosomes, and the Golgi complex, to which endocytic cargo is transported. We then performed 13 small interfering RNA (siRNA) screens of a set of 1,132 genes in parallel (Figure 1A), using pools of three siRNAs per gene (Table S1 available online). The set of selected genes encode for proteins

known or predicted to be central players in signaling networks, represent regulators, and components of membrane-trafficking machineries or that are involved in the regulation of cytoskeleton dynamics (Figure S1A).

After cell and nucleus segmentation, extensive computational image analysis was applied to quantify a multivariate set of features in ~2,500 single cells for each perturbation in each screen (Figure 1B). By means of supervised machine learning, we excluded ~30% of cells, which were mitotic and apoptotic, out-of-focus, and/or poorly segmented, from the data set (Rämö et al., 2009). In addition, perturbations that led to a strong reduction in cell viability (<150 cells/well remaining) were completely excluded from the data set. Furthermore, because hitlists based on multivariate and univariate intensity-based readouts overlap for ~80% (Figure S1B), and changes in single-cell intensity measurements mean the same for each of the 13 readouts, we used single-cell intensity measurements to compare RNAi effects across the 13 screens and to infer functional interactions.

Various experimental and statistical tests (Tables S2 and S3; Figures S1C and S1D) demonstrate high technical reproducibility of the screens. Consistently, we obtained high validation rates of hits found in the screens on amount of intracellular Tfn and LAMP1 abundance in A431 cells using three independent siRNAs from a different supplier (77% and 74%; Table S3). We also verified that established Z- and b-score transformation of the measurements (Boutros et al., 2006) accurately represent the raw data, allowing us to combine all screens into a single data set consisting of a unifying and cross-comparable quantitative readout of single-cell intensities. These tests provided confidence in using the whole data set as a resource for various types of data-driven systems-level analyses. Whenever an individual gene is explicitly mentioned, its RNAi effect has been independently validated (Table S3).

Measuring Direct RNAi Effects at the Single-Cell Level Improves the Data Set

Perturbation effects are usually compared on the basis of averaging single-cell readouts, but this can in many cases be misleading (Altschuler and Wu, 2010). One reason for this is the poor reproducibility of single-cell distributions, leading to inadvertent sampling bias when a few single cells are analyzed. In addition, the silencing of many genes leads to altered properties of a cell population by interfering with cell proliferation or cell migration, leading to changed fractions of densely and sparsely growing cells and cells located on cell islet edges and consequently changed distributions of cell sizes, morphologies, and the extent of cell spreading (Snijder et al., 2012). Because many activities are determined by these single-cell properties (Snijder et al., 2009, 2012), such a perturbation will also alter the single-cell distribution of that activity, without having directly perturbed the activity itself.

To address this, we calculated the number of single cells that must be sampled from a population to obtain a similar distribution of single-cell intensities in two subsamplings and found that, on average across all screens, a sampling of 1,016 single cells is required to achieve a reproducibility (R^2) of 0.9. With an average of 2,500 single cells measured for each perturbation in

each screen, our single-cell sampling size is thus sufficient for the majority of perturbations. We also created statistical models of the population context (Snijder et al., 2012) with good predictive power of single-cell activities ($R = 0.85 \pm 0.16$, median \pm SD), which revealed specific and sometimes strikingly different patterns of cell-to-cell variability (Figure 1C). For instance, the amount of intracellular LDL is higher in cells that are small and grow at high local cell density, whereas the amount of intracellular EGF is high in large, sparsely growing cells. These findings were confirmed in independent experiments in which LDL and EGF uptake were simultaneously monitored in the same cells (Figures S1F and S1G). Correcting the readouts for indirect population context-determined perturbation effects predicted by the models improved the statistical significance of positive controls, which had on average 3-fold higher Z scores (Figure 1D), and increased the statistical separation of hits from nonhits (an average increase in kurtosis of distributions of RNAi effects with 10%) (Figure S1I). Most importantly, the identity of the genes in the top 100 ranking hits across all screens changed considerably (between 27% and 67%, with an average of 40%) (Figure S1H). This led to an increased enrichment of functional annotations of genes with well-known roles in endocytic membrane trafficking, such as the cytoskeleton, secretion, endocytosis, the Ubl (ubiquitin) pathway, vesicle coat formation, organelle localization, and vesicle-mediated transport (Figure 1E), whereas it reduced the enrichment of annotations with expected pleiotropic roles in cellular physiology, such as ribosomal protein and protein import in the nucleus (Figure 1E).

Thus, indirect population context-determined effects are strong confounding factors in RNAi screens of endocytosis and organelle abundance. This must be accounted for in order to better enrich for genes that are directly involved in endocytosis and to allow a meaningful comparison between perturbation effects of endocytic activities that display different population context-determined cell-to-cell variability patterns, such as LDL and EGF uptake.

Systems-Level Insights into the Regulation of the Endocytic Membrane System

To analyze the amount of information that the screens collectively contain, we measured the pairwise correlations between each of the 13 readouts across all direct perturbation effects (Figure S2A). The correlation coefficients ranged from -0.1 to a maximum of 0.44. This shows that each screen provides orthogonal information on the endocytic membrane system. In addition, the pairwise correlation matrix of all screens demonstrated the presence of structure in the data (Figure S2A).

We further studied this emergent property using unsupervised hierarchical clustering of the 13 screens based on the direct perturbation effects of all 1,132 genes, which generated a tree of endocytic activities and organelles (Figure 2A). Reassuringly, Tfn uptake in HeLa and A431 cells cluster together, as does EGF uptake in both cell lines. Thus, although there are cell line-specific effects, these are not dominant in systems-level analyses. From the resulting tree, a subcluster emerges of EEA1 (early endosomes) and LAMP1 (late endosomes/lysosomes) abundance, a subcluster of LDL uptake, macropinocytosis and fluid phase uptake, and a sub-cluster of GM1 abundance on

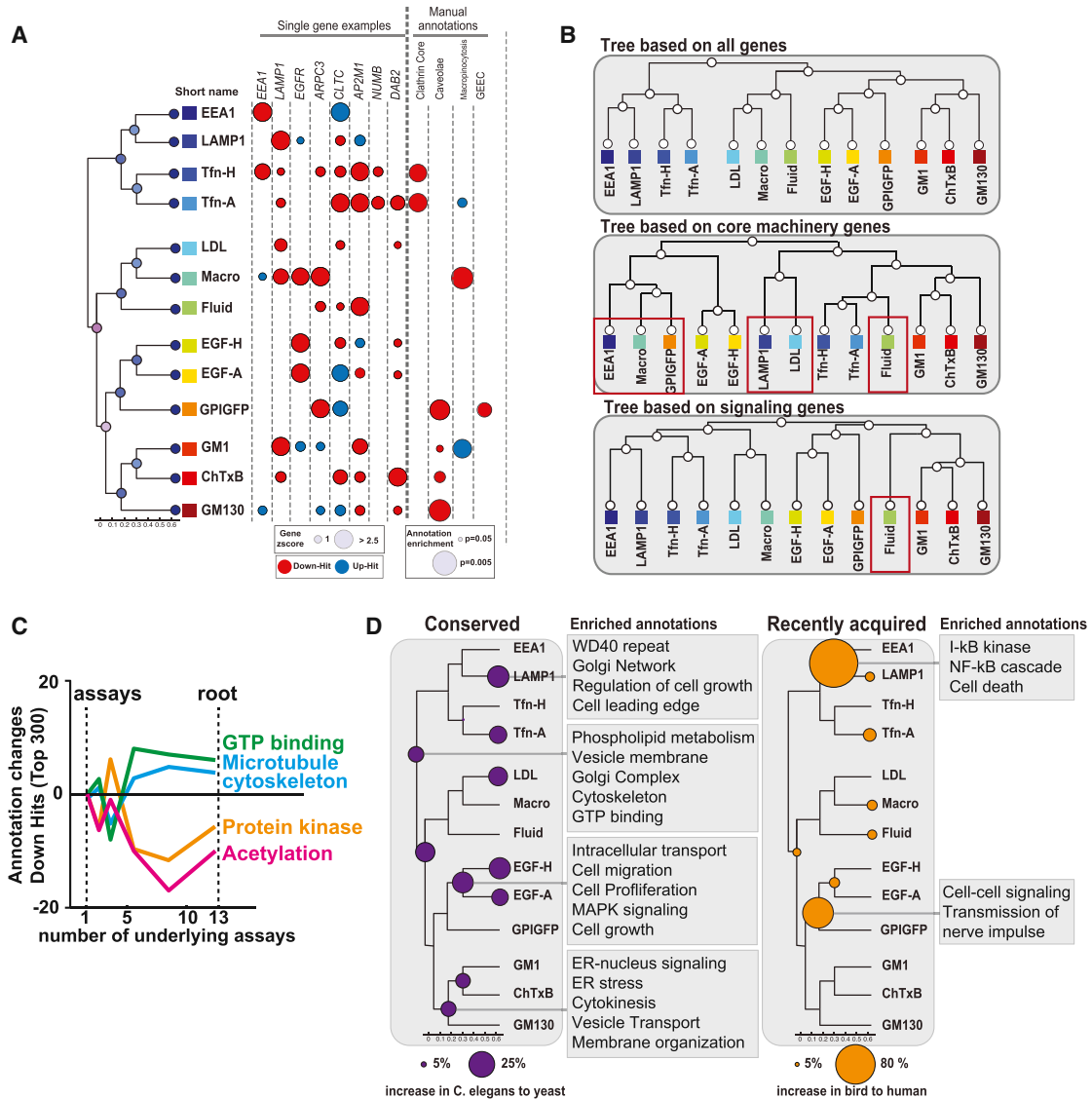


Figure 2. Emergent Properties of the Endocytic Membrane System

(A) Bootstrapped hierarchical clustering of the 13 RNAi screens based on all 1,132 direct RNAi effects. Effects of eight individual well-characterized genes (single gene examples), and enrichment in four manual annotation categories (Table S4) is depicted as circles.

(B) Comparison of three bootstrapped hierarchical clustering results based on direct RNAi effects of different sets of selected genes. Top panel: full data set. Middle panel: selected manual annotations of core endocytic machinery components (Table S4). Bottom panel: all protein and lipid kinases in the human genome.

(C) Annotation enrichments were calculated for each branchpoint of the tree and plotted as a function of the number of underlying screens of individual branchpoints (ranging from one for individual screens to 13 for the root).

(D) Genes were assigned to three evolutionary conservedness classes (conserved, *Caenorhabditis elegans* – *S. cerevisiae*, intermediate conserved, *Danio rerio* – *Drosophila melanogaster*, and recently acquired, *H. sapiens* – *Gallus gallus*), and the number of genes in each class in the top 50 hit list of each screen and each branchpoint of the tree were calculated. Node size indicates the percent increase in genes in a class over the full data set (see legend). Only the classes strongly conserved and recently acquired showed significant increases.

See also Figure S2.

the cell surface, ChTxB uptake, and GM130 (Golgi complex) abundance. Furthermore, GPI-GFP uptake clusters with EGF uptake, and the sub-clusters of Tfn uptake and EEA1-LAMP1 abundance are connected. Numerous single-gene examples with previously characterized roles in endocytosis display the expected profiles of direct RNAi effects across the tree. This,

for instance, illustrates that RNAi of *EEA1*, *LAMP1*, and *EGFR* have their strongest direct effect in the respective readouts that stain for them, which is not the case when population-context effects are not accounted for (data not shown). It also shows that clathrin-mediated endocytosis in these cell lines engages differently and sometimes multiple adaptor proteins,

depending on the cargo. Because these profiles of direct perturbation effects are a unique resource, we facilitate their browsing and comparison on an interactive Web site (<http://www.endocytome.org>).

The main purpose of generating this data set is to reveal systems-level properties of the endocytic membrane system that go beyond the identification of particular genes but that arise from their multiple and complex interactions. Here, we report three emerging properties. First, the subclustering in the tree (Figure 2A) did not clearly separate all clathrin-mediated endocytic activities from clathrin-independent activities. For instance, EGF uptake in both cell lines clustered together, even though it is clathrin-independent in A431 cells. In addition, EGF uptake clustered, somewhat distantly, with GPI-GFP uptake, which is clearly clathrin-independent in our assays. Also, macropinocytosis, another clathrin-independent uptake pathway, clusters with LDL uptake and, more distantly, with fluid phase uptake, which are both, to some extent, clathrin dependent. To understand if different subsets of genes can drive the emergence of a different tree structure, we performed unsupervised clustering with various subsets of genes. Strikingly, a different tree structure emerged when only genes that encode for well-known core machinery components of endocytosis are used (Figure 2B). In this tree, EEA1 abundance clustered with macropinocytosis and GPI-GFP uptake, LDL uptake with LAMP1 abundance, and Tfn uptake in both cell lines with fluid phase uptake. The cluster consisting of GM1 abundance on the cell surface, ChTxB uptake, and GM130 (Golgi complex) abundance did not change. When we generated a tree using only genes encoding for kinases, a structure similar to the one based on all genes emerged, with the exception of fluid phase uptake, which clustered poorly (Figure 2B). This shows that although the endocytic uptake of two ligands may rely on similar core machinery, the regulation of their uptake can be different. Vice versa, the uptake of two ligands may be regulated by similar kinases, but they depend on different core machinery. Although a tree based on genes with well-characterized roles in endocytosis is useful to compare functional patterns of core machinery components, we focus on the tree that emerged from clustering all perturbation effects, which reflects functional patterns of coregulation in the endocytic membrane system.

Second, by calculating enrichments of functional gene annotations among genes whose direct RNAi effects determine the different branchpoints in the tree, we tested whether certain gene functions are more or less common among global regulators of the endocytic membrane system compared to specific regulators of only few endocytic activities or organelle abundances. This revealed that gene functions involved in, for instance, regulating the microtubule cytoskeleton and the action of GTPases are more enriched at the root of the tree, whereas gene functions involved in posttranslational regulation, namely protein kinases and acetylation, are depleted at the root (Figure 2C). Thus, the former are involved in a general regulation of the endocytic membrane system, whereas the latter add specificity to the various endocytic activities and organelles.

Third, by using an evolutionary conservedness score for individual human genes (Ciccarelli et al., 2006) (Figure S2B), we asked how the complexity of the endocytic membrane system

in human cells could have evolved. A significant enrichment in evolutionarily conserved genes was found in genes that define the root of the tree and the first branchpoint above the root, comprising core processes of membrane trafficking, as well as in LAMP1 abundance, LDL uptake, EGF uptake, and the sub-cluster of GM130 abundance, GM1 abundance on the cell surface, and ChTxB uptake, which in addition comprise processes that control the physiological state of cells (Figure 2D). An analysis of recently acquired genes in evolution revealed a highly specific pattern. Particularly, genes controlling both EEA1 and LAMP1 abundance involved in I- κ B kinase, NF- κ B cascade, and cell death and genes controlling GPI-GFP uptake and EGF uptake involved in cell-cell signaling and transmission of nerve impulse are recently acquired in evolution. This shows that a recent evolutionarily acquired mechanism for stress signaling during infection, namely NF- κ B signaling, has been specifically linked to regulating the organelles involved in the uptake of infectious agents. Furthermore, it suggests that cell-cell communication and nerve transmission may have acquired specific properties in higher organisms by involving the endocytic processes that internalize GPI-GFP and EGF.

These analyses show that a broad set of quantitative direct perturbation measurements from a large number of orthogonal readouts of a complex interconnected system, such as endocytosis in human cells, enables the unbiased identification of systems-level insights that conventional approaches cannot reveal. They indicate the existence of specific programs of regulatory control that coordinate subsets of endocytic activities and organelle abundances regardless of the core membrane-traffic machinery on which these activities rely. These programs are enriched in gene functions, such as kinases and acetylation, and are a mix of evolutionarily conserved processes that control the physiological state of cells, as well as regulatory processes recently acquired in evolution. The latter include genes involved in stress signaling during infection and cell-cell communication.

Distinct Programs of Regulatory Control in the Endocytic Membrane System

To further characterize these regulatory programs, we identified functional annotations that enrich in genes coregulating the activities in the subclusters of the tree (Table S4). For easy comparison, we visualized particularly enriched functional annotation categories as a network in which the size and the color represent enrichment and average RNAi effect, respectively (Figures 3A–3E). Comparing the resulting patterns shows that EEA1 and LAMP1 abundance are specifically cosuppressed by genes involved in cell size growth and differentiation. This may suggest that these regulatory programs suppress the endolysosomal system to reduce the extent of plasma membrane remodeling and membrane degradation in order to maintain a more stabilized cell-surface composition, which is essential for cell differentiation, to sustain cell-surface signaling, and to allow cells to grow in size.

Another important set of interconnected annotation categories comprises stress signaling, c-Jun terminal kinases (JNK), and different levels of mitogen signaling. Tfn uptake is promoted by all of these signaling activities, whereas EGF and GPI-GFP uptake are copromoted in particular by kinases that are more

downstream in the MAPK signaling pathway. GM1 cell-surface abundance, ChTxB uptake, and GM130 abundance in contrast are copromoted by upstream signaling, such as the regulation of stress and MAPKKK signaling. A strikingly opposite pattern is found for the subcluster of LDL uptake and macropinocytosis, which is cosuppressed by these signaling activities. The purpose of this anticorrelated coregulation of endocytic activities by this major signaling axis in proliferating cells is yet unknown. One possibility is that it promotes endocytic activities that contribute to mitogenic and stress signaling, whereas it suppresses endocytic activities that would attenuate such signaling.

Genes involved in cell adhesion differentially control subsets of endocytic activities and organelle abundances. Cell adhesion promotes EEA1 and LAMP1 abundance, as well as LDL uptake and macropinocytosis, whereas it suppresses EGF and GPI-GFP uptake. The latter is consistent with the existence of extensive crosstalk between cell adhesion and growth factor signaling in anchorage-dependent growth. Finally, genes inducing lipid biosynthesis promote Tfn uptake as well as LDL uptake and macropinocytosis, which are connected to genes involved in insulin signaling that promote LDL uptake and macropinocytosis. STAT3 signaling specifically promotes Tfn uptake.

This shows that regulatory programs linked to multiple aspects of the physiological state of cells (such as cell size, proliferation, differentiation, and adhesion) and triggered by extracellular growth factors and cytokines (and thus active in tissue culture cells grown in serum) separate the endocytic membrane system into different groups of coregulated endocytic activities and organelle abundances. This grouping emerged from an unbiased approach based on the direct RNAi effects of 1,132 genes involved in signaling, membrane trafficking, and the cytoskeleton and is different from one that is based solely on genes that encode for well-characterized endocytic machinery components. This indicates that even when the endocytic uptake of different ligands is dependent on similar core machinery, the regulation of this machinery according to the physiological state of cells can be substantially different.

Properties of Hierarchical Functional Interactions between Genes in Yeast and Human Cells

To explore the above findings in greater depth requires the inference of functional interactions between individual genes at a large scale. This would allow us to map how signaling genes that define these regulatory programs functionally interact with genes encoding for the molecular machinery of endocytosis and to analyze higher-level properties of these genetic interactions, including network motifs. The current gold standard in inferring functional interactions between individual genes at a large scale relies on double-gene perturbation screens in yeast and bacteria (Costanzo et al., 2010; Nichols et al., 2011; Schuldiner et al., 2005). These approaches have been highly successful in mapping the genetic interaction landscape in these organisms and identifying numerous functional protein complexes by calculating the pairwise correlation between genes across a large set of epistatic effects with other genes (Costanzo et al., 2010; Nichols et al., 2011; Schuldiner et al., 2005). However, correlations are less suitable to infer regulatory interactions

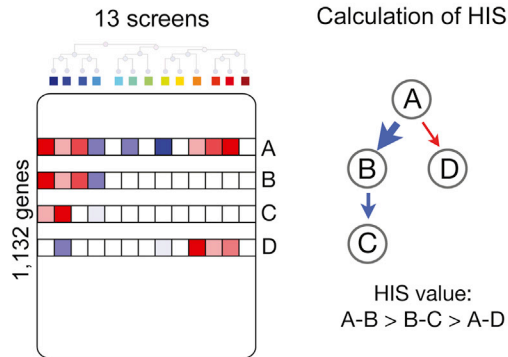
between genes, such as kinases and their substrates, because they often do not show consistent effects over large numbers of readouts or synthetic interactions (Fiedler et al., 2009). Thus, a statistical method that identifies subset effects, in which one gene shows perturbation effects that are a subset of those of another gene, might be better suited. In addition, such a method may be useful for identifying functional interactions between endocytic machinery components that only cofunction in a subset of activities, such as between clathrin and specific adaptor proteins.

To address this, we developed a statistical approach that infers interactions when overall good correlations are found and perturbation effects are strong, but, importantly, also when similarities in subset effects are observed, from which it in addition infers a statistical hierarchy (Figure 4A) (Snijder et al., 2013). This method, termed the hierarchical interaction score (HIS), greatly outperforms correlation-based methods in inferring functional interactions from parallel single-gene perturbation screens in both *Drosophila* and human cells and performs equally well in inferring functional interactions from synthetic double-gene knockout screens in yeast (Snijder et al., 2013).

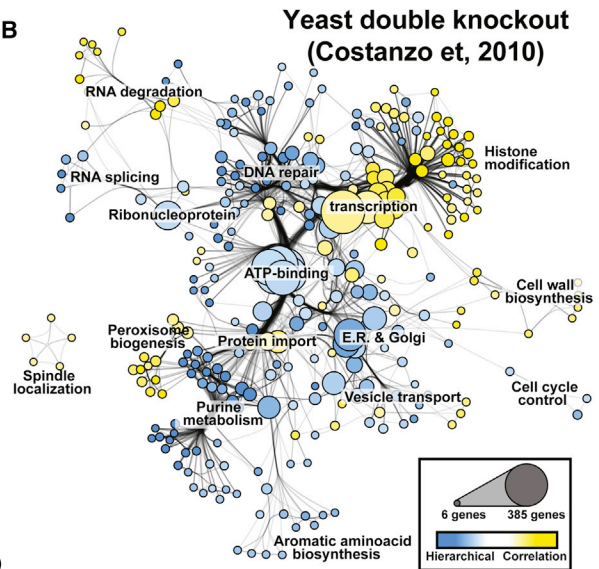
To systematically evaluate the power of the HIS, we first calculated HIS interaction scores from a large set of synthetic interactions in yeast (Costanzo et al., 2010). HIS interaction scores higher than zero were obtained for 257,807 combinations (1.72%) between 3,876 *S. cerevisiae* genes (Figure S3). Because correlation-based methods work well on the yeast data set, we could compare enrichments in functional annotations of genes connected by the HIS and by correlation. Strikingly, the two inference methods are to a large extent complementary and connect genes that enrich in different cellular processes. For instance, ATP-binding (mainly kinases), endoplasmic reticulum and Golgi, and vesicle transport contain significantly more hierarchical than correlation-based interactions (Figure 4B). In addition, the HIS infers more regulatory interactions between cellular processes, in particular between kinases, membrane trafficking, and the cytoskeleton, whereas overall correlation identifies more interactions within functional annotations of multisubunit complexes, such as the ribosome (Figure 4C) or the proteasome (data not shown). Thus, the HIS reveals the type of functional interactions that we are concerned with in this study.

Next, we calculated HIS interaction scores from our data set (see Figure 4A) for each of the 1.28 million possible pairwise combinations between the 1,132 genes. For 55,070 combinations (4%) between 969 genes, a score higher than zero was found (Figure S3; Table S5; Data S1), indicating a functional interaction. When we compared HIS interactions from the yeast and our data set, we could identify numerous interactions that were present in both (Data S1), some of which were confirmed in an independent database on functional gene and protein interactions (STRING v. 9.0). In one example, functional interactions were found between membrane-trafficking machinery (*RAB7A*, *ALIX*, and *VPS39*), actin-binding proteins (*CAPZA1*, *CAPZB*), and mitogen-activated protein kinases (*MAPK1* and *MAPK7*) (Figure 4D). Interestingly, the conserved example revealed an interaction motif, known as Fan-In, in which two genes (or sets of genes) converge on a downstream gene (or set of genes). In fact, we found that this motif is the most abundant among all

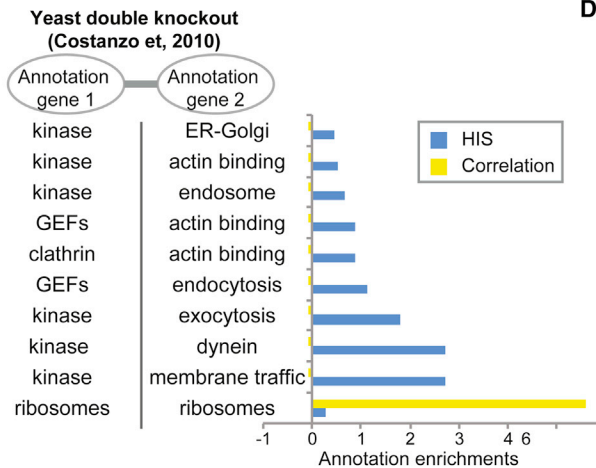
A



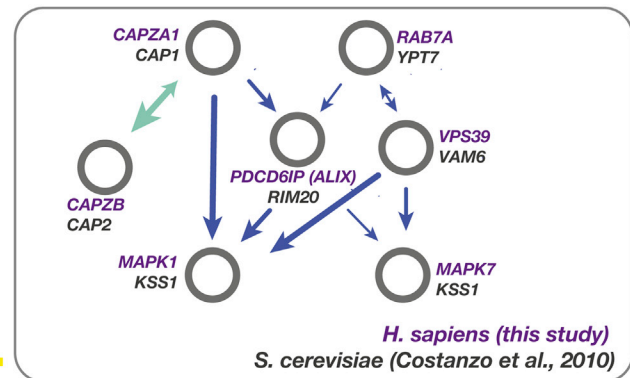
B



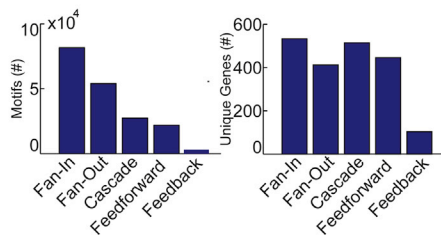
C



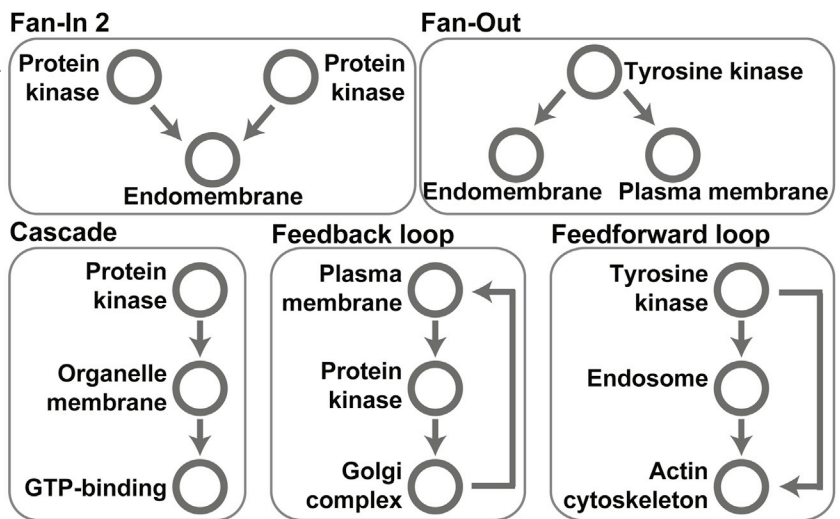
D



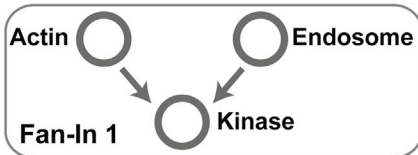
E



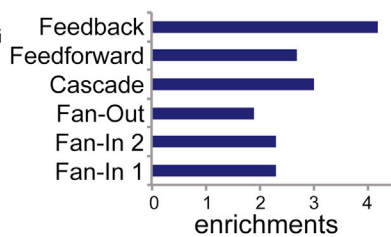
H



F



G



(legend on next page)

possible hierarchical interaction motifs between three genes in our data set (Figure 4E). A subsequent analysis of functional annotation enrichments among genes connected in the Fan-In hierarchical interaction motif revealed that integration of actin and membrane-trafficking machinery to downstream kinases, like the conserved example mentioned above (Figure 4F), as well as the integration of two upstream kinases to downstream membrane trafficking machinery (Figure 4G), is commonly used. Performing this enrichment analysis on the other hierarchical interaction motifs identified in our data set revealed numerous additional types of commonly used regulation: tyrosine kinases upstream of both endomembrane and plasma membrane (Fan-Out motif), plasma membrane proteins interacting via protein kinases with the Golgi complex, which in turn interact with the plasma membrane (Feedback motif), and tyrosine kinases that are both directly upstream of actin cytoskeleton components and indirectly upstream via endosome components, integrating these two annotation groups (Feedforward motif).

Taken together, comparing HIS with correlation-based interactions from a yeast synthetic interaction data set revealed that both methods are largely complementary, but HIS-based functional networks are superior in providing insights into the systems-level organization of regulatory interactions in cells. Many cellular processes contain numerous hierarchical interactions that have thus far not been uncovered, such as regulatory interactions between membrane trafficking, the cytoskeleton, and signaling. In addition, hierarchical interaction motifs inferred from our data set suggest the existence of generic regulatory principles in the endocytic membrane system.

A Map of Hierarchical Functional Interactions between Signaling and Membrane Trafficking Genes in Human Cells

We next selected HIS interactions from our data set with a score of 0.3 or higher (between 132 genes; 13.6% of all genes predicted to interact) (Figure 5A). At this threshold, only strong outliers in the full distribution of interaction scores are considered (0.5% of all predicted interactions; p value: 6.2×10^{-154}) (Figure 5A), collectively showing the highest enrichment in databases of known functional associations between genes and

thus displaying the most significant predictive power (Figure S4A). We then created a pairwise HIS map of these 132 genes using all inferred HIS interaction values and clustered the genes based on their profile of HIS interactions. This revealed a set of distinct clusters with a strong modular structure (Figures 5B and S4B for a high-resolution map with gene labels), which we color-coded according to the subset of screens that contribute in determining the interaction. Like correlation-based genetic interaction maps (Schuldiner et al., 2005), this map identifies clusters of genes with similar HIS interaction profiles across a large number of genes and with HIS interactions among each other (blocks along the diagonal) and reveals genes that act as connectors of distinct modules (horizontal or vertical stripes of HIS interactions away from the diagonal). An important difference between the two methods is that a HIS map is not fully symmetric, reflecting the directionality in the inferred interactions.

To study some of the properties of the HIS map in more detail, we created a functional interaction network between the 132 genes using 247 functional interactions (HIS value ≥ 0.3 , p value: 6.2×10^{-154}) (Figure 5C). The connections in this network are similarly color-coded as in the HIS map (see color legend of the endocytic tree), and the thickness of the interaction reflects the interaction score. Many connections are directional, reflecting the statistical hierarchy of a broader set of effects being upstream of a subset of effects. Some connections are bidirectional, which indicates the absence of a statistical hierarchy and are seen in tight clusters (Data S1). The HIS network reflects the strong modular structure visible in the HIS map, with clusters of genes functionally interconnected based on subsets of endocytic activities and organelles, and a number of genes, which link these subclusters. Below, we mention four examples of interconnected genes, which control different subsets of activities in the tree.

The first example (Figure 6A), which promotes EGF and GPI-GFP uptake, consists of *EGFR*, *PIP5K3*, *SNX6*, and *MAP3K11*. *EGFR* lies upstream of *PIP5K3* (PIKFYVE), consistent with EGF signaling stimulating the production of PI(3,5)P₂ (Tsujita et al., 2004), which lies upstream of *SNX6*, as this component of the retromer requires PI(3,5)P₂ for membrane recruitment (Rutherford et al., 2006). The second example promotes GM1 abundance at the cell surface and ChTxB uptake, consisting of

Figure 4. Systems Properties of Hierarchical Interactions in Yeast and Human Cells

(A) Schematic of the principle underlying the calculation of the hierarchical interaction score (HIS). Directionality is inferred from the gene with the broader set of effects to the gene with the narrower set of effects. The strength of the interactions (HIS value; thickness of the arrows) reflects the extent to which subset effects are similar.

(B) Systematic comparison of functional annotation enrichments in genes connected by the HIS and by correlation inferred from a large double-gene perturbation screen in *S. cerevisiae* (Costanzo et al., 2010). Functional annotations (nodes in the network) are connected (gray line) when at least 20% of the genes overlap. The size of each node indicates the number of genes in an annotation category and the color a relative enrichment in HIS- (blue) versus correlation-based (yellow) interactions.

(C) Comparison of inferred interactions in the yeast data set between genes with different functional annotations. Bar graphs show the enrichments for specific connections between functional annotations inferred by the HIS (blue) and by correlation (yellow).

(D) Example of functional interactions only inferred by the HIS in both data sets and confirmed in an independent database. Edges between nodes are color-coded depending on the subset of screens in this study that contributed most in determining the interaction.

(E) Number of three-gene HIS interaction motifs and number of unique genes in each motif inferred from the data set collected in this study.

(F) Enriched Fan-In motif between genes with depicted functional annotations to which the conserved example in (D) belongs.

(G and H) Enrichments and examples of selected interaction motifs between functional gene annotations of signaling, membrane trafficking, and the cytoskeleton.

See also Figure S3.

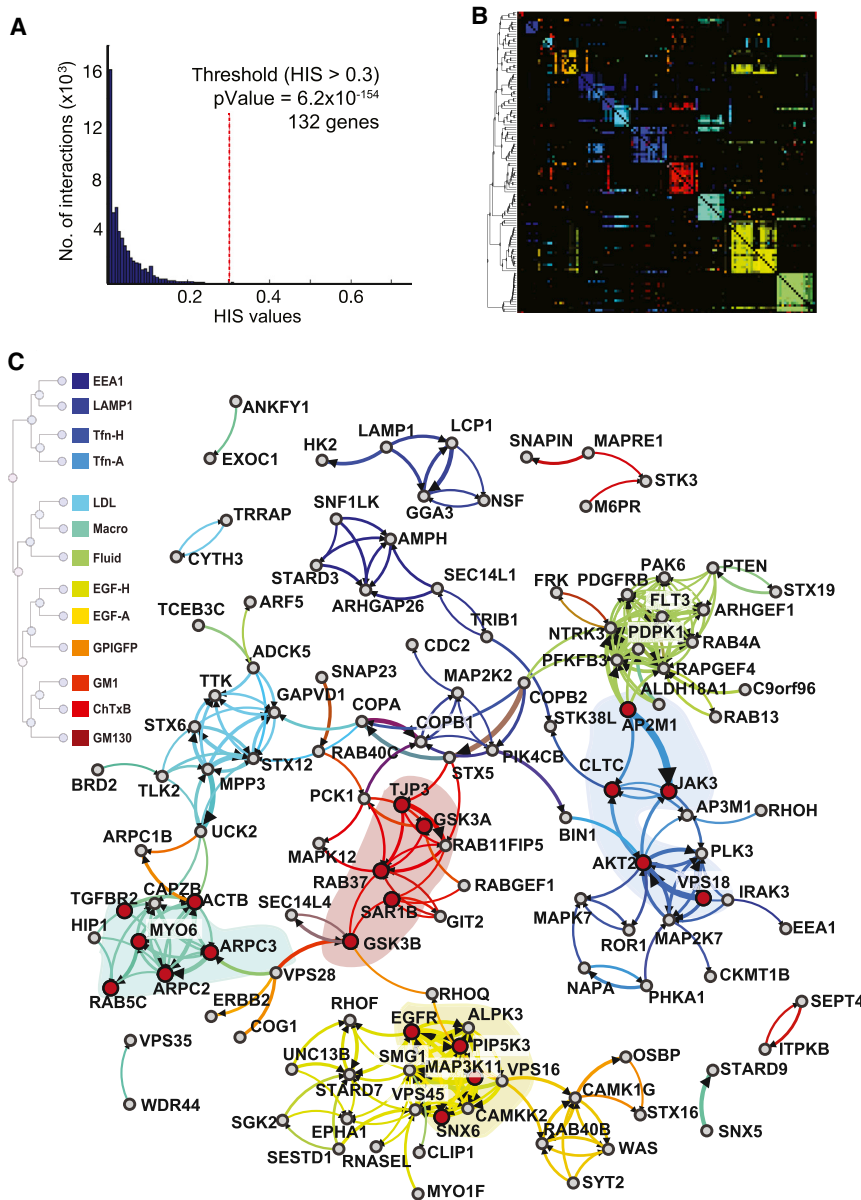


Figure 5. A Map of Regulatory Functional Interactions in the Endocytic Membrane System

(A) Distribution of HIS interactions between 969 genes calculated from the 13 RNAi screens. The number of HIS interactions with the value ≥ 0.3 are 247 (red dashed line in distribution) (p value: 6.2×10^{-154}), connecting 132 genes that have at least one HIS interaction above this threshold.

(B) A full HIS map of all HIS values between these 132 genes is depicted, color-coded according to the subset of screens that determined the interaction.

(C) Network visualization of the 247 HIS interactions with values ≥ 0.3 between 132 genes. Edges between nodes are color-coded depending on the subset of screens that contributed most in determining the interaction (see legend). See also Figure S4.

actin, which interacts with the minus-end-directed actin motor Myosin-6. Interestingly, the HIS predicts that the Arp2/3 complex and Myosin-6 functionally interact with *RAB5C*, which acts as a macropinocytosis-specific isoform of Rab5. The fourth example contains functional interactions between *VPS18*, *AP2M1*, *AKT2*, *JAK3*, and *CLTC*, which regulate the uptake of Tfn (Figure 6D) and is further discussed below.

Although it is difficult to estimate the true-positive rate of the 247 functional interactions in this map, $\sim 30\%$ of them link genes that are functionally coannotated; $\sim 8\%$ of them match known functional interactions between proteins (Figure S4). This is 3- to 4-fold higher than what correlation-based methods can predict from parallel RNAi screens in human or *Drosophila* cells and reach about half the estimated true-positive

rate of both correlation-based and HIS interactions inferred from synthetic interaction screens in yeast and bacteria (Costanzo et al., 2010; Nichols et al., 2011; Snijder et al., 2013). The inferred interactions reveal known regulatory mechanisms, and the hierarchy holds functional information. When we tested a number of specific kinase inhibitors in Tfn uptake, we found that specifically the inhibitors of *AKT2* and *JAK3* strongly reduce Tfn uptake in HeLa and A431 cells (Figure 6E), whereas the other tested kinase inhibitors had no or milder effects. This is consistent with the fact that the strongest predicted functional interactions from our data set for kinases controlling Tfn uptake were downstream of *AKT2* and *JAK3* (see Figure 5, blue connections). Because many connections in the network are uncharacterized, they provide a resource for studying mechanisms of the regulatory molecular interplay between signaling and endocytosis.

GSK3A, *GSK3B*, *SAR1B*, *RAB37*, and *TJP3* (Figure 6B). Here, the two isoforms of *GSK3* and *TJP3* are upstream of *RAB37*, and *GSK3B* is upstream of *SAR1B*. *GSK3*, a serine/threonine kinase, is critically important in the beta-catenin/Wnt signaling pathway (Clevers, 2006), whereas *RAB37* mediates the secretion of post-Golgi secretory granules (Brunner et al., 2007), and *SAR1B* has a central role in vesicle transport from the endoplasmic reticulum to the Golgi complex. In a third example, we find *TGFBR2*, *ARPC2*, *ARPC3*, *ACTB*, *MYO6*, and *RAB5C* promoting macropinocytosis (Figure 6C). *TGFBR2* functions upstream of *ARPC2* and *ACTB* (Moustakas and Stouraras, 1999), which connect to *ARPC3* and *MYO6*. *ARPC2* and *MYO6* also connect to *RAB5C*. This places TGF-beta receptor signaling in control of macropinocytosis by functionally interacting with the Arp2/3 complex, which mediates actin polymerization, and beta-

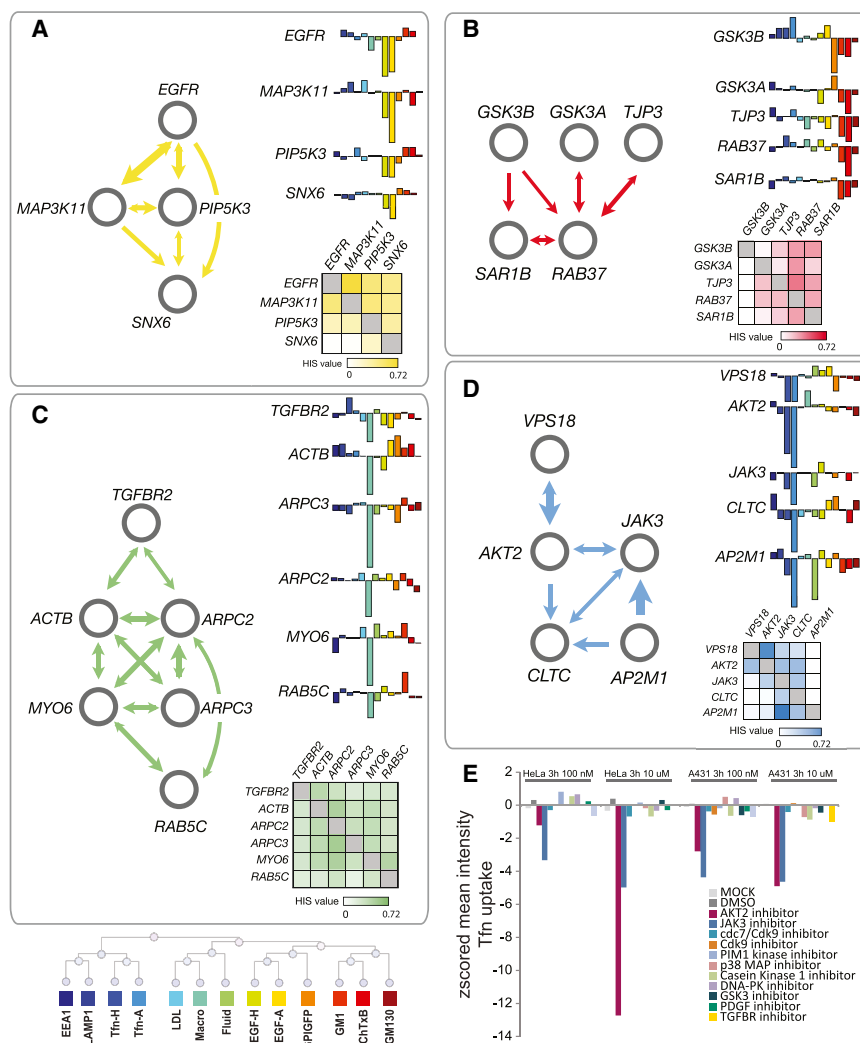


Figure 6. Examples of Predicted Regulatory Functional Interactions and Validation

(A–D) Selected examples of predicted HIS interactions. Shown are HIS subnetworks inferred from the direct RNAi effects across the endocytic tree (color-coded bar graphs), based on all pairwise HIS values between the genes (see heatmaps; rows are forward interactions, and columns are reverse interactions), resulting in either fully directional interactions, asymmetric bidirectional interactions, and fully bidirectional interactions, and color-coded depending on the subset of screens that contributed most in determining the interaction (see legend).

(E) Z score mean intensity per cell (normalized with the mean and SD of DMSO controls) of intracellular TfR after 15 min uptake in HeLa and A431 cells pretreated for 3 hr with different inhibitors (see legend).

Compared to the control, the CCPs in AKT2-inhibited cells contain similar amounts of CLTA but much less DNM2 (Figures 7C, 7D, and S5D) and more TfR (Figure S5E). The CCPs in JAK3-inhibited cells contain more CLTA and DNM2 (see Figures 7C, 7D, and S5D for full distributions) and strongly accumulate TfR (Figure S5E). This suggests that AKT2 activity promotes the recruitment of DNM2 during maturation of CCPs, whereas JAK3 activity promotes the internalization of DNM2-positive CCPs.

We then studied the dynamics of CCPs and focused on two types of events (Figure 7E): unproductive formation of a CCP, where CLTA appears and disappears without transient recruitment of DNM2,

and productive formation and internalization of a CCP, where CLTA appears and only disappears simultaneously with DNM2 upon its latter recruitment. We developed a computational method to obtain time traces of 50,000 productive events. This shows an average lifetime of CCPs of 120 s from initial recruitment of CLTA to productive internalization by DNM2, as previously reported (Loerke et al., 2009) (Figure 7F). Both inhibitors decrease the rate of productive internalization events (Figure 7G) and increase the lifetime of clathrin-coated pits on the cell surface (Figure 7H), but the effect of the JAK3 inhibitor is stronger. Furthermore, in those internalization events that were still productive, more DNM2 was recruited to the CCP in JAK3-inhibited cells compared to untreated cells, whereas this was not the case in AKT2-inhibited cells (Figure 7I).

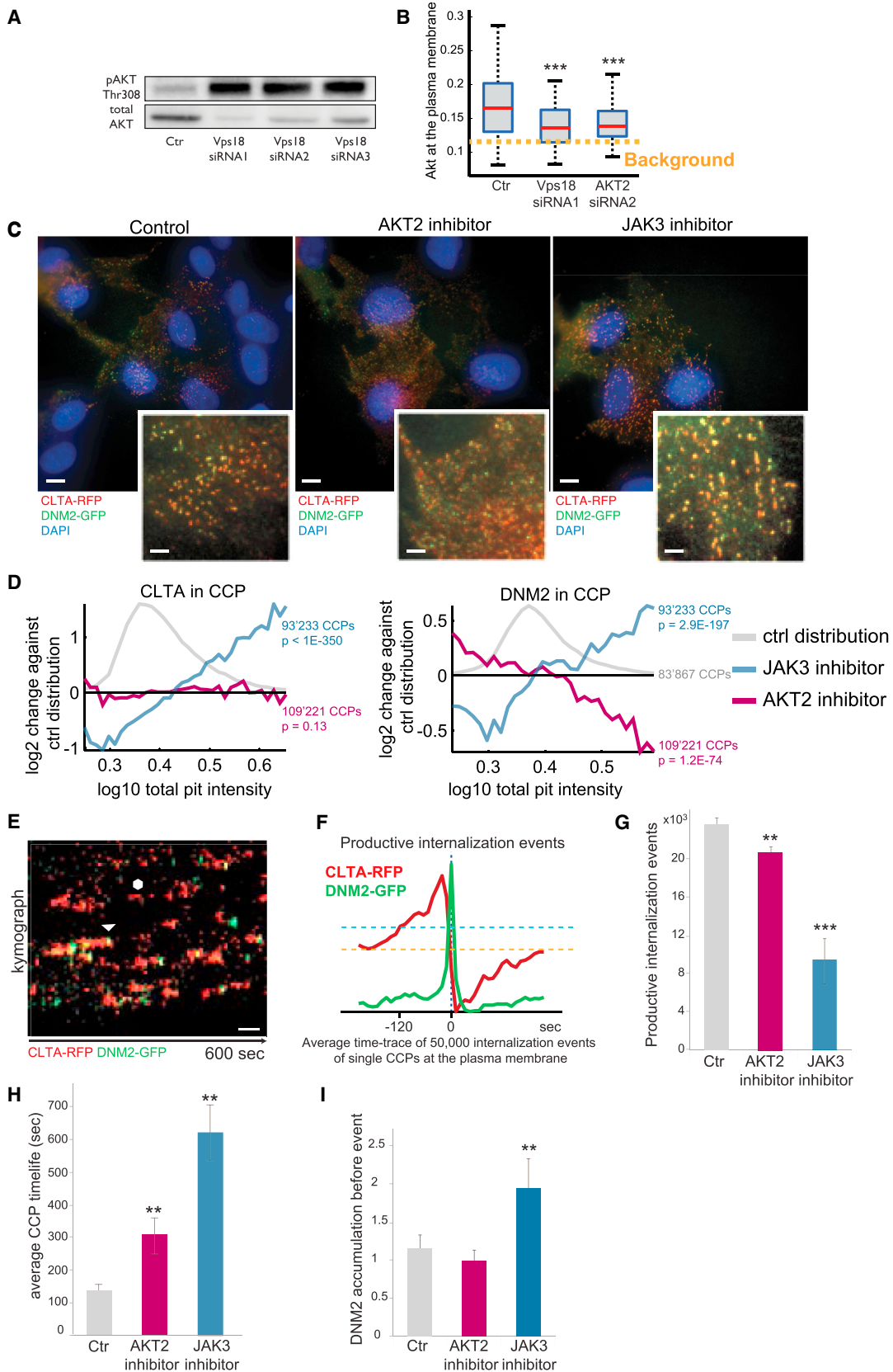
DISCUSSION

In this study, we perturb, by means of RNAi, a selected set of human genes involved in signal transduction, membrane trafficking, and the cytoskeleton and quantify the effects on the

Characterizing a Subnetwork of Functional Interactions

We characterized in more detail the functional interactions between *VPS18*, *AKT2*, and *CLTC* and between *JAK3* and *CLTC*. RNAi of *VPS18* reduces the level of total AKT and strongly increases the amount of phosphorylated AKT at both Thr308 (Figure 7A) and Ser423 (data not shown). Quantitative TIRF microscopy revealed that under these conditions total AKT (Figure 7B) and phosphorylated AKT at Thr308 (Figure S5A) are strongly depleted from the plasma membrane. *VPS18* might control levels and localization of AKT by recruiting AKTIP on endosomes (Richardson et al., 2004), consistent with a role for local entrapment of activated AKT2 on endosomes to protect it from degradation (Walz et al., 2010).

We next applied automated large-scale three-color TIRF imaging of >430 genome-edited cells with endogenously tagged CLTA-RFP and DNM2-GFP (Doyon et al., 2011), combined with cell segmentation and automated detection of >55,000 clathrin-coated pits (CCPs), to determine the number of CCPs per cell and measure distributions of CCP content. Both inhibitors cause a strong increase in the number of CCPs per cell (Figure S5C).



(legend on next page)

endocytic membrane system with orthogonal readouts from 13 high-throughput image-based screens. Quantifying a large number of single cells per perturbation and population context modeling allowed a quantitative and meaningful comparison of direct perturbation effects. This enabled the discovery of unknown systems properties of the endocytic membrane system in human cells. We demonstrate the existence of specific programs of regulatory control that coordinate subsets of endocytic activities and organelle abundances regardless of the core membrane-trafficking machinery on which these activities rely. The programs are a mix of evolutionary conserved processes that control the physiological state of cells, as well as processes recently acquired in evolution, such as stress signaling during infection and cell-cell communication. They consist of specific combinations of signaling pathways and subdivide the endocytic membrane system into five groups of coregulated endocytic activities and organelle abundances.

To explore these regulatory programs in greater depth, we applied a statistical method, termed the hierarchical interaction score (HIS) (Snijder et al., 2013), that uses subset effects in the data to infer, at a large scale, a type of functional interaction between genes, which are hierarchical and contain directionality. These interactions allowed the large-scale identification of regulatory motifs between signaling, membrane trafficking, and cytoskeletal genes and suggest a widespread use of signal integration, as well as feedback and feedforward mechanisms. Importantly, the inferred directionality in the interaction or interaction motif represents a statistical hierarchy between two or multiple perturbation effects present in the data. More work will be necessary to understand how this statistical hierarchy relates to biochemical directionality and what the roles of hierarchical interaction motifs are in molecular terms. Nevertheless, it represents a resource for systems biology research in membrane trafficking, analogous to how gene regulatory network motifs have been important for understanding systems properties of transcription (Alon, 2007). Examples show that this sheds light onto the interactions between growth factor signaling, membrane recycling machinery, the actin cytoskeleton and early endosome trafficking, and between beta-catenin/Wnt signaling and the secretory pathway. In addition, a more

detailed experimental characterization of a subset of predicted hierarchical interactions reveals that intracellular endosome machinery controls clathrin-mediated endocytosis at the cell surface via the serine/threonine kinase AKT2, which promotes maturation and dynamin recruitment to clathrin-coated pits, whereas the serine/threonine kinase JAK3, involved in cytokine signaling, promotes productive internalization of mature clathrin-coated pits.

Hierarchical functional genetic interactions are also ubiquitous in *S. cerevisiae*. They can be inferred from double-gene perturbation screens, representing a class of functional regulatory interactions that have been largely unknown. Many cellular processes contain more hierarchical than correlation-based interactions, indicating a general property of the functional genetic organization of cells. This property goes beyond the interactions between membrane trafficking, signaling, and the cytoskeleton and applies to processes such as DNA repair, RNA splicing, cell-cycle control, and metabolism. We expect that the types of information that can be retrieved with maps of hierarchical interactions are manifold, of which only a fraction has been explored here. Our approach will be generally applicable, including to large-scale gene knockout screens in human cells (Mali et al., 2013; Shalem et al., 2014), and complementary to conventional genetic interaction screening to decipher complex and heavily regulated cellular processes across organisms.

EXPERIMENTAL PROCEDURES

Details of all experimental and computational procedures are described in the [Extended Experimental Procedures](#). All previously published MatLab code and CellProfiler modules are available on <http://www.infectome.org>. The data set can be browsed online at <http://www.endocytome.org>.

Development of Image-Based Screens

Cells were plated in 384-well plates for reverse transfection with siRNA pools and subsequently grown for 3 days in complete medium to establish efficient knockdown of the targeted genes. At the end of each assay, cells were permeabilized for 5 min with 0.1% Triton X-100 at room temperature (RT) and stained for 5 min at RT with DAPI and Cell Trace. After final washing, cells were kept in PBS for imaging. For more details, see the [Extended Experimental Procedures](#).

Figure 7. Characterization of Predicted Regulatory Functional Interactions

- (A) Western blot of total AKT and Thr308-phosphorylated AKT after RNAi of *VPS18* with three independent siRNAs.
- (B) TIRF microscopy analysis of AKT localization at the plasma membrane after RNAi of *VPS18* or *AKT2*. Box plots indicate the AKT staining intensity in the TIRF channel, quantified in 1,131 cells from three independent experiments. ***p value < 10^{-10} .
- (C) Selected TIRF microscopy images of CLTA-RFP and DNM2-GFP genome-edited SK-MEL-2 cells treated with DMSO, AKT2-specific inhibitor, or JAK3-specific inhibitor. Scale bars, 20 μm ; enlargement, 7 μm .
- (D) Quantification of the amount of CLTA and DNM2 in CCPs in cells treated with the AKT2 or JAK3 inhibitor. Log₂-fold differences in their intensity distributions in CCPs compared to their intensity distributions in control cells are shown.
- (E) Kymograph of CCP dynamics in CLTA-RFP and DNM2-GFP genome-edited SK-MEL-2 cells shows productive (white triangle) and unproductive (white hexagon) events.
- (F) Large-scale automated analysis of 50,000 productive internalization events in 29 cells. Depicted is the average time trace of the Z score signal of CLTA and DNM2. Blue dashed line: significant accumulation of CLTA in CCPs. Orange dashed line: background intensity in the CLTA channel.
- (G) Quantification of productive internalization events ($\text{sec}/\mu\text{m}^2$) in control (54,906 events, 29 cells), AKT2 inhibitor-treated (30,093 events, 25 cells), and JAK3 inhibitor-treated cells (12,356 events, 17 cells). Depicted are cell-averaged values \pm SD. **p value < 0.02, ***p value < 0.001.
- (H) Bar graph showing CCP lifetimes, measured as the time before the internalization event at which CLTA is significantly accumulated in CCPs. Depicted are cell-averaged values \pm SD. **p value < 0.02.
- (I) Bar graph quantifying the amount of DNM2 accumulated in CCPs before the internalization event, measured as the sum of DNM2 intensity in the last 50 s before internalization. Depicted are cell-averaged values \pm SD. **p value < 0.006 (all p values are two-tailed t tests).

See also [Figure S5](#).

High-Content Single-Cell Imaging of Populations of Cells

We imaged 384-well plates with a wide-field 20× objective microscope (ImageExpress Micro, Molecular Devices). We acquired five focal planes per image and 30 sites per well. The maximum intensity projection of the five focal planes was saved for each site and used for further analysis. The 2.1×10^6 images (6TB) collected in the primary and secondary screens were stored as 16-bit uncompressed TIFFs.

Image Analysis Pipeline, Single-Cell Feature Extraction, and Supervised Machine Learning for Data Quality Control

For image analysis and single-cell feature extraction, we used the open-source software package Cell Profiler (Carpenter et al., 2006), extended with custom-made image analysis modules for the measurement of cell population-context features (Snijder et al., 2009, 2012). For supervised classification of cellular phenotypes based on support vector machines, we used custom software (Rämö et al., 2009). In total we extracted ~200 features per single cell, resulting in 5TB of single-cell measurements. For detailed information about features extracted from single cells, see the [Extended Experimental Procedures](#).

Clustering, Functional Annotation Enrichments, Inference of Functional Interactions, and Identifying Network Motifs

Detailed descriptions of these computational approaches can be found in the [Extended Experimental Procedures](#).

SUPPLEMENTAL INFORMATION

Supplemental Information includes Extended Experimental Procedures, five figures, one data file, and five tables and can be found with this article online at <http://dx.doi.org/10.1016/j.cell.2014.04.029>.

ACKNOWLEDGMENTS

We thank Y. Heer, N. Battich, B. Thijssen, M. Stark, C. von Meering, and K. Mench for help with experiments and computation, Y. Yakimovich for IT support, and lab members for comments on the manuscript. P.L. is supported by a FEBS. L.P. acknowledges financial support from the SystemsX.ch Research, Technology, and Development projects PhosphoNetX and LipidX and the University of Zurich.

Received: September 12, 2013

Revised: January 30, 2014

Accepted: April 10, 2014

Published: June 5, 2014

REFERENCES

- Alon, U. (2007). Network motifs: theory and experimental approaches. *Nat. Rev. Genet.* 8, 450–461.
- Altschuler, S.J., and Wu, L.F. (2010). Cellular heterogeneity: do differences make a difference? *Cell* 141, 559–563.
- Bassik, M.C., Kampmann, M., Lebbink, R.J., Wang, S., Hein, M.Y., Poser, I., Weibezahn, J., Horlbeck, M.A., Chen, S., Mann, M., et al. (2013). A systematic mammalian genetic interaction map reveals pathways underlying ricin susceptibility. *Cell* 152, 909–922.
- Boutros, M., Brás, L.P., and Huber, W. (2006). Analysis of cell-based RNAi screens. *Genome Biol.* 7, R66.
- Brunner, Y., Couté, Y., Iezzi, M., Foti, M., Fukuda, M., Hochstrasser, D.F., Wollheim, C.B., and Sanchez, J.C. (2007). Proteomics analysis of insulin secretory granules. *Mol. Cell. Proteomics* 6, 1007–1017.
- Carpenter, A.E., Jones, T.R., Lamprecht, M.R., Clarke, C., Kang, I.H., Friman, O., Guertin, D.A., Chang, J.H., Lindquist, R.A., Moffat, J., et al. (2006). CellProfiler: image analysis software for identifying and quantifying cell phenotypes. *Genome Biol.* 7, R100.
- Ciccarelli, F.D., Doerks, T., von Mering, C., Creevey, C.J., Snel, B., and Bork, P. (2006). Toward automatic reconstruction of a highly resolved tree of life. *Science* 311, 1283–1287.
- Clevers, H. (2006). Wnt/beta-catenin signaling in development and disease. *Cell* 127, 469–480.
- Collinet, C., Stöter, M., Bradshaw, C.R., Samusik, N., Rink, J.C., Kenski, D., Habermann, B., Buchholz, F., Henschel, R., Mueller, M.S., et al. (2010). Systems survey of endocytosis by multiparametric image analysis. *Nature* 464, 243–249.
- Conner, S.D., and Schmid, S.L. (2003). Regulated portals of entry into the cell. *Nature* 422, 37–44.
- Costanzo, M., Baryshnikova, A., Bellay, J., Kim, Y., Spear, E.D., Sevier, C.S., Ding, H., Koh, J.L.Y., Toufighi, K., Mostafavi, S., et al. (2010). The genetic landscape of a cell. *Science* 327, 425–431.
- Doherty, G.J., and McMahon, H.T. (2009). Mechanisms of endocytosis. *Annu. Rev. Biochem.* 78, 857–902.
- Fiedler, D., Braberg, H., Mehta, M., Chechik, G., Cagney, G., Mukherjee, P., Silva, A.C., Shales, M., Collins, S.R., van Wageningen, S., et al. (2009). Functional organization of the *S. cerevisiae* phosphorylation network. *Cell* 136, 952–963.
- Galvez, T., Teruel, M.N., Heo, W.D., Jones, J.T., Kim, M.L., Liou, J., Myers, J.W., and Meyer, T. (2007). siRNA screen of the human signaling proteome identifies the PtdIns(3,4,5)P3-mTOR signaling pathway as a primary regulator of transferrin uptake. *Genome Biol.* 8, R142.
- Hillenmeyer, M.E., Fung, E., Wildenhain, J., Pierce, S.E., Hoon, S., Lee, W., Proctor, M., St Onge, R.P., Tyers, M., Koller, D., et al. (2008). The chemical genomic portrait of yeast: uncovering a phenotype for all genes. *Science* 320, 362–365.
- Kozik, P., Hodson, N.A., Sahlender, D.A., Simecek, N., Soromani, C., Wu, J., Collinson, L.M., and Robinson, M.S. (2013). A human genome-wide screen for regulators of clathrin-coated vesicle formation reveals an unexpected role for the V-ATPase. *Nat. Cell Biol.* 15, 50–60.
- Laufer, C., Fischer, B., Billmann, M., Huber, W., and Boutros, M. (2013). Mapping genetic interactions in human cancer cells with RNAi and multiparametric phenotyping. *Nat. Methods* 10, 427–431.
- Liberali, P., Rämö, P., and Pelkmans, L. (2008). Protein kinases: starting a molecular systems view of endocytosis. *Annu. Rev. Cell Dev. Biol.* 24, 501–523.
- Loerke, D., Mettlen, M., Yarar, D., Jaqaman, K., Jaqaman, H., Danuser, G., and Schmid, S.L. (2009). Cargo and dynamin regulate clathrin-coated pit maturation. *PLoS Biol.* 7, e57.
- Mali, P., Yang, L., Esvelt, K.M., Aach, J., Guell, M., DiCarlo, J.E., Norville, J.E., and Church, G.M. (2013). RNA-guided human genome engineering via Cas9. *Science* 339, 823–826.
- Maxfield, F.R., and McGraw, T.E. (2004). Endocytic recycling. *Nat. Rev. Mol. Cell Biol.* 5, 121–132.
- Moustakas, A., and Stourmaras, C. (1999). Regulation of actin organisation by TGF-beta in H-ras-transformed fibroblasts. *J. Cell Sci.* 112, 1169–1179.
- Nichols, R.J., Sen, S., Choo, Y.J., Beltrao, P., Zietek, M., Chaba, R., Lee, S., Kazmierczak, K.M., Lee, K.J., Wong, A., et al. (2011). Phenotypic landscape of a bacterial cell. *Cell* 144, 143–156.
- Pelkmans, L., Fava, E., Grabner, H., Hannus, M., Habermann, B., Krausz, E., and Zerial, M. (2005). Genome-wide analysis of human kinases in clathrin- and caveolae/raft-mediated endocytosis. *Nature* 436, 78–86.
- Rämö, P., Sacher, R., Snijder, B., Begemann, B., and Pelkmans, L. (2009). CellClassifier: supervised learning of cellular phenotypes. *Bioinformatics* 25, 3028–3030.
- Richardson, S.C., Winistorfer, S.C., Poupon, V., Luzio, J.P., and Piper, R.C. (2004). Mammalian late vacuole protein sorting orthologues participate in early endosomal fusion and interact with the cytoskeleton. *Mol. Biol. Cell* 15, 1197–1210.
- Roguev, A., Talbot, D., Negri, G.L., Shales, M., Cagney, G., Bandyopadhyay, S., Panning, B., and Krogan, N.J. (2013). Quantitative genetic-interaction mapping in mammalian cells. *Nat. Methods* 10, 432–437.

- Rutherford, A.C., Traer, C., Wassmer, T., Pattni, K., Bujny, M.V., Carlton, J.G., Stenmark, H., and Cullen, P.J. (2006). The mammalian phosphatidylinositol 3-phosphate 5-kinase (PIKfyve) regulates endosome-to-TGN retrograde transport. *J. Cell Sci.* *119*, 3944–3957.
- Schuldiner, M., Collins, S.R., Thompson, N.J., Denic, V., Bhamidipati, A., Punna, T., Ihmels, J., Andrews, B., Boone, C., Greenblatt, J.F., et al. (2005). Exploration of the function and organization of the yeast early secretory pathway through an epistatic miniarray profile. *Cell* *123*, 507–519.
- Scita, G., and Di Fiore, P.P. (2010). The endocytic matrix. *Nature* *463*, 464–473.
- Shalem, O., Sanjana, N.E., Hartenian, E., Shi, X., Scott, D.A., Mikkelsen, T.S., Heckl, D., Ebert, B.L., Root, D.E., Doench, J.G., and Zhang, F. (2014). Genome-scale CRISPR-Cas9 knockout screening in human cells. *Science* *343*, 84–87.
- Snijder, B., Sacher, R., Rämö, P., Damm, E.-M., Liberali, P., and Pelkmans, L. (2009). Population context determines cell-to-cell variability in endocytosis and virus infection. *Nature* *461*, 520–523.
- Snijder, B., Sacher, R., Rämö, P., Liberali, P., Mench, K., Wolfrum, N., Burleigh, L., Scott, C.C., Verheije, M.H., Mercer, J., et al. (2012). Single-cell analysis of population context advances RNAi screening at multiple levels. *Mol. Syst. Biol.* *8*, 579.
- Snijder, B., Liberali, P., Frechin, M., Stoeger, T., and Pelkmans, L. (2013). Predicting functional gene interactions with the hierarchical interaction score. *Nat. Methods* *10*, 1089–1092.
- Steinman, R.M., Mellman, I.S., Muller, W.A., and Cohn, Z.A. (1983). Endocytosis and the recycling of plasma membrane. *J. Cell Biol.* *96*, 1–27.
- Steinmetz, L.M., Scharfe, C., Deutschbauer, A.M., Mokranjac, D., Herman, Z.S., Jones, T., Chu, A.M., Giaever, G., Prokisch, H., Oefner, P.J., and Davis, R.W. (2002). Systematic screen for human disease genes in yeast. *Nat. Genet.* *31*, 400–404.
- Tsujita, K., Itoh, T., Ijuin, T., Yamamoto, A., Shisheva, A., Laporte, J., and Takenawa, T. (2004). Myotubularin regulates the function of the late endosome through the gram domain-phosphatidylinositol 3,5-bisphosphate interaction. *J. Biol. Chem.* *279*, 13817–13824.
- Walz, H.A., Shi, X., Chouinard, M., Bue, C.A., Navaroli, D.M., Hayakawa, A., Zhou, Q.L., Nadler, J., Leonard, D.M., and Corvera, S. (2010). Isoform-specific regulation of Akt signaling by the endosomal protein WDFY2. *J. Biol. Chem.* *285*, 14101–14108.